

Calculation of isotope shifts and relativistic shifts in CI, CII, CIII and CIV

J. C. Berengut*

School of Physics, University of New South Wales, Sydney 2052, Australia

V. V. Flambaum

School of Physics, University of New South Wales, Sydney 2052, Australia and

*Physics Division, Argonne National Laboratory,
Argonne, Illinois 60439-4843, USA*

M. G. Kozlov

Petersburg Nuclear Physics Institute, Gatchina, 188300, Russia

(Dated: June 10, 2021)

Abstract

We present an accurate *ab initio* method of calculating isotope shifts and relativistic shifts in atomic spectra. We test the method on neutral carbon and three carbon ions. The relativistic shift of carbon lines may allow them to be included in analyses of quasar absorption spectra that seek to measure possible variations in the fine structure constant α over the lifetime of the Universe. Carbon isotope shifts can be used to measure isotope abundances in gas clouds: isotope abundances are potentially an important source of systematic error in the α -variation studies. These abundances are also needed to study nuclear reactions in stars and supernovae, and test models of chemical evolution of the Universe.

PACS numbers: 31.30.Gs, 06.20.-f, 31.25.Jf

Keywords: isotope shift; mass shift; relativistic shift; carbon

*Electronic address: jcb@phys.unsw.edu.au

I. INTRODUCTION

Recent studies of quasar absorption systems have suggested that the fine structure constant, $\alpha = e^2/\hbar c$, may have been smaller in the early universe than it is today on Earth [1, 2, 3, 4]. Other groups using different telescopes have shown zero variation [5, 6, 7]. All of these studies use the “many multiplet” method [8], which relies on the comparison of the wavelengths of many transitions in many ions to enhance the size of the effects and remove sources of systematic error. While this method offers an order-of-magnitude improvement in sensitivity over the previously used alkali-doublet method, a potential systematic error is introduced related to the isotope abundances of the absorbers. If the isotope abundances of the absorbers differ from the terrestrial abundances then there can be spurious shifts in the measured wavelengths which may be incorrectly interpreted as variation of α .

This problem can be resolved if both the relativistic shift and isotope shift of each transition is known, by using particular combinations of the transition frequencies as probes which are insensitive to either α -variation or isotopic abundances [9]. Changes in the isotope abundances and the fine-structure constant can then be measured directly.

The measured isotopic abundance of carbon can be used to test models of chemical evolution of the Universe. Of particular importance are some chemical evolution models with enhanced populations of intermediate-mass stars that serve as factories for heavy Mg isotopes. The changes in the relative abundances of Mg isotopes could account for much of the evidence for variation in α at relatively low redshifts ($z \lesssim 2$) [10, 11]. However, these models also overproduce nitrogen, violating observed abundance trends in high- z damped Lyman- α systems. Furthermore, it has been shown that such models would also increase the ratio of ^{13}C to ^{12}C [12]. With the isotope shifts calculated in this paper it is possible to measure this ratio, and hence provide a diagnostic of these non-standard chemical evolution models.

We also have one more reason to study carbon: it is a well studied atom, and we can compare the results of our method with those of other theoretical analyses, as well as a few experiments (unfortunately, isotope shifts for the majority of lines used in astrophysical applications have not been measured). In particular, much progress has been made to calculate isotope shifts using the multiconfigurational Hartree-Fock (MCHF) and configuration interaction (CI) approach [13, 14, 15, 16]. In Sections II and III we present our method of calculating the isotope shift. It uses the finite-field method to reduce the problem of isotope shift (or relativistic shift) to that of an energy calculation. The transition energies are calculated using a combination of the configuration interaction and many-body perturbation theory (MBPT) approaches, following the works of Refs. [17] and [18].

In Sec. IV we show that our CI + MBPT method has accuracy comparable to that of the MCHF calculations, and are accurate enough to be used to measure isotope abundances. We believe that our method may have some advantages over the MCHF calculations; in particular, it is more readily applicable to heavier atoms (where we need to calculate isotope shifts for the study of the α variation and isotopic evolution) and has already been shown to be more accurate in the case of Mg I [19]. We also use this method to calculate dependence of the carbon transition frequencies on α , which is needed to study α variation.

II. METHOD

Using many-body perturbation theory in the residual Coulomb operator and specific mass shift (SMS) operator to calculate isotope shift shows poor convergence. Therefore, we are looking for an “all order” method of calculation. The finite-field scaling method is used, reducing the task to an energy calculation, and including the SMS in all parts of the calculation. A similar idea is used to calculate relativistic shift.

A. Relativistic shift

To measure α in the distant past, we compare the frequency of transitions in the laboratory, ω_0 , with those measured in the quasar absorption spectra, ω . The difference can be expressed as

$$\omega = \omega_0 + qx, \quad (1)$$

where $x = (\alpha/\alpha_0)^2 - 1$ and α_0 is the laboratory value of the fine structure constant. We vary α directly in computer codes, and extract the relativistic shift q from the calculated spectrum as

$$q = \left. \frac{d\omega}{dx} \right|_{x=0}. \quad (2)$$

Thus we have reduced the problem to an accurate numerical calculation of the energy, and hence ω .

B. Isotope shift

The isotope shifts of atomic transition frequencies come from two sources: the finite size of the nuclear charge distribution (the “volume” or “field” shift), and the finite mass of the nucleus (see, e.g., Ref. [20]). In atoms as light as carbon, the field shift is negligible in comparison to the mass shift: we will not consider it further.

Because a real nucleus has a finite mass, there is a recoil effect from the movements of the electrons. The energy shift due to the recoil of the nucleus of mass M is given by

$$\begin{aligned} \frac{\mathbf{p}_N^2}{2M} &= \frac{1}{2M} \left(\sum_i \mathbf{p}_i \right)^2 \\ &= \frac{1}{2M} \sum_i p_i^2 + \frac{1}{M} \sum_{i<j} \mathbf{p}_i \cdot \mathbf{p}_j. \end{aligned} \quad (3)$$

This “mass shift” is traditionally divided into the normal mass shift (NMS) and the specific mass shift (SMS), given by the first and second terms of Eq. (3), respectively. The normal mass shift is easily calculated from the transition frequency; the specific mass shift is difficult to evaluate accurately.

The shift in energy of any transition in an isotope with mass number A' with respect to an isotope with mass number A can be expressed as

$$\delta\nu^{A',A} = \nu^{A'} - \nu^A = (k_{\text{NMS}} + k_{\text{SMS}}) \left(\frac{1}{A'} - \frac{1}{A} \right), \quad (4)$$

where the normal mass shift constant is

$$k_{\text{NMS}} = -\frac{\nu}{1823}. \quad (5)$$

The value 1823 refers to the ratio of the atomic mass unit to the electron mass.

To calculate k_{SMS} we include a scaled specific-mass-shift operator directly into our energy calculation from the very beginning. We add the two-body SMS operator to the Coulomb potential $\tilde{Q} = 1/|\mathbf{r}_1 - \mathbf{r}_2| + \lambda \mathbf{p}_1 \cdot \mathbf{p}_2$. The operator \tilde{Q} replaces the Coulomb operator everywhere that it appears in an energy calculation. We recover the specific mass shift constant as

$$k_{\text{SMS}} = \left. \frac{d\omega}{d\lambda} \right|_{\lambda=0}. \quad (6)$$

The operator \tilde{Q} has the same symmetry and structure as the Coulomb operator (see Appendix A).

III. ENERGY CALCULATION

To calculate the energies we first solve the Dirac-Fock equations for the core and valence electrons, and we generate a basis set that includes the core and valence orbitals and a number of virtual orbitals. We then calculate the energy levels using a combination of CI and MBPT for many-valence-electron atoms as was done for Mg I in Ref. [19]. In this section we outline the procedure for the combined CI and MBPT method; it generally follows the work of Ref. [17]. Note that for single-valence-electron atoms, where the CI procedure is unnecessary, the method reduces to the addition of core-correlation effects to the Dirac-Fock energy using MBPT, as was shown to be highly successful for calculating SMS in Ref. [21]. Atomic units ($\hbar = m_e = e = 1$) are used throughout this paper.

A. Single particle basis

We firstly solve the Dirac-Fock equations for one-particle wavefunctions of the open-shell core $|m\rangle$

$$h^{\text{DF}} |m\rangle = \epsilon_m |m\rangle, \quad (7)$$

where

$$h^{\text{DF}} = c \boldsymbol{\alpha} \cdot \mathbf{p} + (\beta - 1)m_e c^2 - \frac{Z}{r} + V^{\text{NDF}}(r) \quad (8)$$

where V^{NDF} is the potential (both direct and exchange) of the N_{DF} electrons included in the self-consistent Hartree-Fock procedure. Note that this is not necessarily the number of electrons in the closed-shell core, in fact $N_{\text{core}} \leq N_{\text{DF}} \leq N$, where N is the total number of electrons. For the purposes of the CI calculation there are $N - N_{\text{core}}$ valence electrons.

We need to generate a basis set, $|i\rangle$ that includes the core and valence states and a large number of virtual states. In this paper we have used a B-spline basis set, formed by diagonalizing the Dirac-Fock operator on the basis set of B-splines and excluding orbitals with high energy. This basis has been shown to be effective in energy calculations using this method of CI and MBPT [18].

B. Configuration interaction method

The many-electron Hilbert space is separated into subspaces P and Q . P corresponds to the frozen-core approximation; Q is complimentary to it and includes all states with core excitations. Using Slater determinants (denoted with capital letters) $|I\rangle$ of the single-particle functions $|i\rangle$ as a basis set in the many-electron space, we can define projection operators for P and Q by

$$\begin{aligned}\mathcal{P} &= \sum_{I \in P} |I\rangle \langle I| \\ \mathcal{P} + \mathcal{Q} &= 1\end{aligned}\tag{9}$$

Determinants that have all core states fully occupied are in the P subspace; all others are in the subspace Q .

In the CI method, the many-electron wavefunction is expressed as a linear combination of Slater determinants from the subspace P :

$$\psi = \sum_{I \in P} C_I |I\rangle,\tag{11}$$

where the C_I are obtained from the matrix eigenvalue problem

$$\sum_{J \in P} H_{IJ} C_J = E C_I.\tag{12}$$

In the frozen-core approximation, the determinants $|I\rangle$ need include only the valence electrons. Although P is infinite-dimensional, we can use a finite-dimensional model subspace by specifying the set of allowed configurations for the valence electrons, for example by restricting the set of single particle states. The restrictions we use are different for each ion, and are expressed more fully in the relevant parts of Section IV. We will not distinguish here between the finite and infinite subspaces.

The Hamiltonian for the CI problem is a projection of the exact Hamiltonian \mathcal{H} onto the model subspace. The core is frozen in the P subspace, so our projected Hamiltonian is

$$\mathcal{P}\mathcal{H}\mathcal{P} = E_{\text{core}} + \sum_{i > N_{\text{core}}} h_i^{\text{CI}} + \sum_{j > i > N_{\text{core}}} \frac{1}{r_{ij}}\tag{13}$$

where E_{core} is the total energy of the N_{core} core electrons and the single particle operator

$$h^{\text{CI}} = c \boldsymbol{\alpha} \cdot \mathbf{p} + (\beta - 1) m_e c^2 - \frac{Z}{r} + V^{\text{Ncore}}\tag{14}$$

acts only on the valence electrons. Using the operator (13) in Eq. (12) corresponds to the pure CI method in the frozen-core approximation.

C. Exact Hamiltonian expansion

We wish to write the exact equivalent of \mathcal{H} in the subspace P . The ‘‘Feshbach operator’’ yields the exact energy when operating on the model function $\Psi_P = \mathcal{P}\Psi$. Following Lindgren and Morrison [22], we start from the many-body Schrödinger equation in the form

$$\mathcal{H}(\mathcal{P} + \mathcal{Q})\Psi = E\Psi\tag{15}$$

and operate from the left with \mathcal{P} and \mathcal{Q} , respectively to obtain

$$\begin{aligned}\mathcal{P}\mathcal{H}\mathcal{P}\Psi_P + \mathcal{P}\mathcal{H}\mathcal{Q}\Psi_Q &= E\Psi_P \\ \mathcal{Q}\mathcal{H}\mathcal{P}\Psi_P + \mathcal{Q}\mathcal{H}\mathcal{Q}\Psi_Q &= E\Psi_Q.\end{aligned}$$

Eliminating Ψ_Q ,

$$[\mathcal{P}\mathcal{H}\mathcal{P} + \Sigma(E)]\Psi_P = E\Psi_P \quad (16)$$

where

$$\Sigma(E) = \mathcal{P}\mathcal{H}\mathcal{Q}\frac{1}{E - \mathcal{Q}\mathcal{H}\mathcal{Q}}\mathcal{Q}\mathcal{H}\mathcal{P}. \quad (17)$$

In Ref. [17] these expressions were also used to rewrite the orthonormality conditions for the solutions of Eq. (15) in terms of the model functions Ψ_P (the solutions of Eq. (16)). As they found however, if an appropriate choice of the P subspace is made, the usual orthonormality condition for Ψ_P can be applied. In this case the standard CI procedure can be used to solve Eq. (16).

D. Many-body perturbation theory

Here we will generate a perturbation expansion for Σ . Define a single particle Hamiltonian by

$$\begin{aligned}h_0 a_i^\dagger |0\rangle &= \epsilon_i a_i^\dagger |0\rangle \\ \epsilon_i &\equiv \langle i | h^{\text{DF}} | i \rangle.\end{aligned} \quad (18)$$

where we introduce the operators a_i^\dagger (a_i) to create (annihilate) a particle. For particles in the core, the functions are those of Eq. (7). The many-body zero-order Hamiltonian is

$$\mathcal{H}_0 = E_{\text{core}} + \sum_i \{a_i^\dagger a_i\} \epsilon_i. \quad (19)$$

where the brackets $\{\dots\}$ denote normal ordering with respect to the closed-shell core.

The exact Hamiltonian is

$$\mathcal{H} = \sum_i h^{\text{nuc}} + \sum_{i<j} \frac{1}{r_{ij}} \quad (20)$$

where $h^{\text{nuc}} = c\boldsymbol{\alpha} \cdot \mathbf{p} + (\beta - 1)m_e c^2 - \frac{Z}{r_i}$. \mathcal{H} can be separated into zero, one, and two-body parts:

$$\begin{aligned}\mathcal{H}^{(0)} &= E_{\text{core}} \\ \mathcal{H}^{(1)} &= \sum_{ij} \{a_i^\dagger a_j\} \left[\langle i | h^{\text{nuc}} | j \rangle \right. \\ &\quad \left. + \sum_m^{\text{core}} \left(\langle im | r_{12}^{-1} | jm \rangle - \langle im | r_{12}^{-1} | mj \rangle \right) \right] \\ &= \sum_{ij} \{a_i^\dagger a_j\} \langle i | h^{\text{CI}} | j \rangle\end{aligned} \quad (21)$$

$$\mathcal{H}^{(2)} = \sum_{ijkl} \{a_i^\dagger a_j^\dagger a_l a_k\} \langle ij | r_{12}^{-1} | kl \rangle. \quad (22)$$

Expanding Eq. (17) in the residual Coulomb interaction, $\mathcal{V} = \mathcal{H} - \mathcal{H}_0$, we obtain

$$\begin{aligned} \Sigma(E) &= \mathcal{P}\mathcal{H}\mathcal{Q}\frac{1}{E - \mathcal{H}_0}\mathcal{Q}\mathcal{H}\mathcal{P} \\ &+ \mathcal{P}\mathcal{H}\mathcal{Q}\frac{1}{E - \mathcal{H}_0}\mathcal{Q}\mathcal{V}\mathcal{Q}\frac{1}{E - \mathcal{H}_0}\mathcal{Q}\mathcal{H}\mathcal{P} + \dots \end{aligned} \quad (23)$$

One advantage of this formalism is that h_0 is not necessarily the same as h^{DF} . Thus we may in principle use any set of functions we like in the virtual basis as long as they are orthogonal. In practice, however, it is important that \mathcal{V} not get too large, and this requires that

$$\mathcal{V}^{(1)} = \langle i | h^{\text{CI}} - h_0 | j \rangle \quad (24)$$

is small.

We can write Σ in matrix form:

$$\begin{aligned} \Sigma_{IJ} &= \sum_{M \in Q} \frac{\langle I | H | M \rangle \langle M | H | J \rangle}{E - E_M} \\ &+ \sum_{M, L \in Q} \frac{\langle I | H | M \rangle \langle M | V | L \rangle \langle L | H | J \rangle}{(E - E_M)(E - E_L)} + \dots \end{aligned} \quad (25)$$

$$= (\Sigma_2)_{IJ} + (\Sigma_3)_{IJ} + \dots \quad (26)$$

where I and J enumerate determinants from the subspace P , and M and L are determinants from the subspace Q .

In this paper we calculate Σ to second-order of the perturbation expansion. For the one-valence-electron case it has been shown that this level of perturbation theory, when used with the finite-field scaling method, is sufficient to obtain accurate results for isotope shift [21]. Furthermore, previous studies have shown that energies calculated to this order are very accurate [17, 18].

Substituting Σ_2 into (16) we obtain the equation of the combined CI and MBPT method, which we write in the same form as Eq. (12):

$$\sum_{J \in P} \left(H_{IJ} + \sum_{M \in Q} \frac{\langle I | H | M \rangle \langle M | H | J \rangle}{E - E_M} \right) C_J = EC_I. \quad (27)$$

Thus our method includes the core-correlation effects by simply altering the matrix elements in the CI calculation. In practice, this involves adding the matrix element of the sigma operator to the one and two-particle Coulomb integrals.

E. Diagrammatic technique for calculating Σ

Here we present all second-order diagrams for Σ , represented by Goldstone diagrams (see, e.g.: Ref. [22]). The diagrams are valid for any ion and any choice of core. Unlinked lines are omitted, since they correspond to states of the valence electrons that are not involved in the interaction. The omitted lines do affect the value of the MBPT correction via the Pauli principle; however, as noted in Ref. [17], the Pauli principle can be ignored due to the exact cancellation of unphysical terms in different diagrams. This rule works for all orders of perturbation theory (this is Wick's theorem, see e.g.: Ref. [22]).

The second-order diagrams can be grouped according to how many external lines (valence electrons) they have. There are four one-valence-electron diagrams, all shown in Fig. 1. They correspond to the “self-energy” correction, which describes correlations between the valence electron and the core. Additionally, there are five so-called “subtraction diagrams” for the self-energy. These are diagrams that involve the external field $\mathcal{V}^{(1)}$ (Eq. (24)), and are so named because in the Hartree-Fock field enters $\mathcal{V}^{(1)}$ with a minus sign. In our formulation we instead use $\mathcal{H}^{(1)}$ as the external field (see Eqs. (21) and (25)) which is equivalent when calculating Σ_2 because $\mathcal{P}\mathcal{H}_0\mathcal{Q} = 0$. Three of the $\Sigma^{(1)}$ subtraction diagrams are shown in Fig. 2; the other two are the mirror image partners of diagrams 2.1 and 2.2.

FIG. 1: One-valence-electron diagrams of Σ ($\Sigma^{(1)}$).

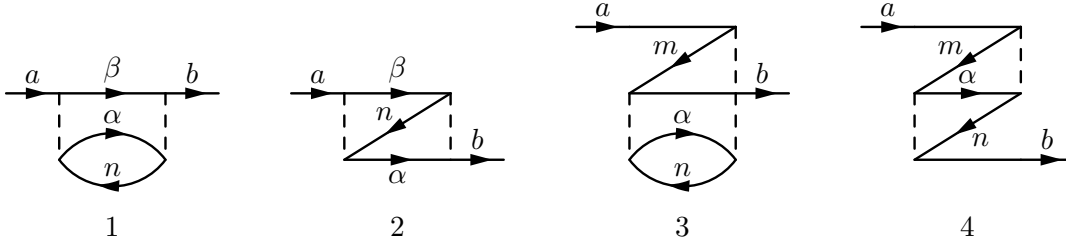
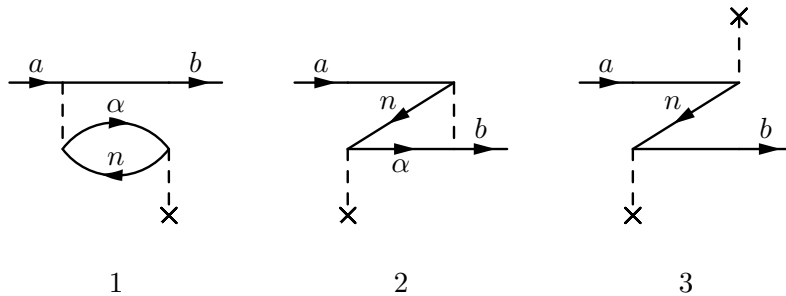


FIG. 2: Subtraction diagrams of $\Sigma^{(1)}$. Diagrams 1 and 2 have complementary diagrams obtained by reflection in the vertical plane.



Diagrams with two external lines correspond to screening of the valence-valence interaction by the core electrons. There are nine diagrams represented in Fig. 3, and four subtraction diagrams represented in Fig. 4. The resulting corrections to the interactions between valence electrons can be written in the form of an effective radial integral, as is usually done for the Coulomb integrals. However, it is important to note that the box diagrams (Figs. 3.4 – 3.6) have less symmetry than the Coulomb integrals, because swapping the initial and final states in either the upper or lower lines changes the integral. This approximately doubles the number of independent radial integrals that need to be stored for the CI problem. In addition, for the box diagrams the multipolarity of the Coulomb interaction need not follow the usual rule: $\xi(l_a + l_c + k)\xi(l_b + l_d + k)$ (see Appendix A). Instead, k need only satisfy the triangle conditions and can be both odd and even. This would again double the number of independent radial integrals, except that we have found that the diagrams of “wrong” parity are unimportant for carbon and may be omitted in order to reduce the complexity of the calculations.

FIG. 3: $\Sigma^{(2)}$: Diagrams 1, 2 and 3 have complementary diagrams obtained by reflection in the vertical plane.

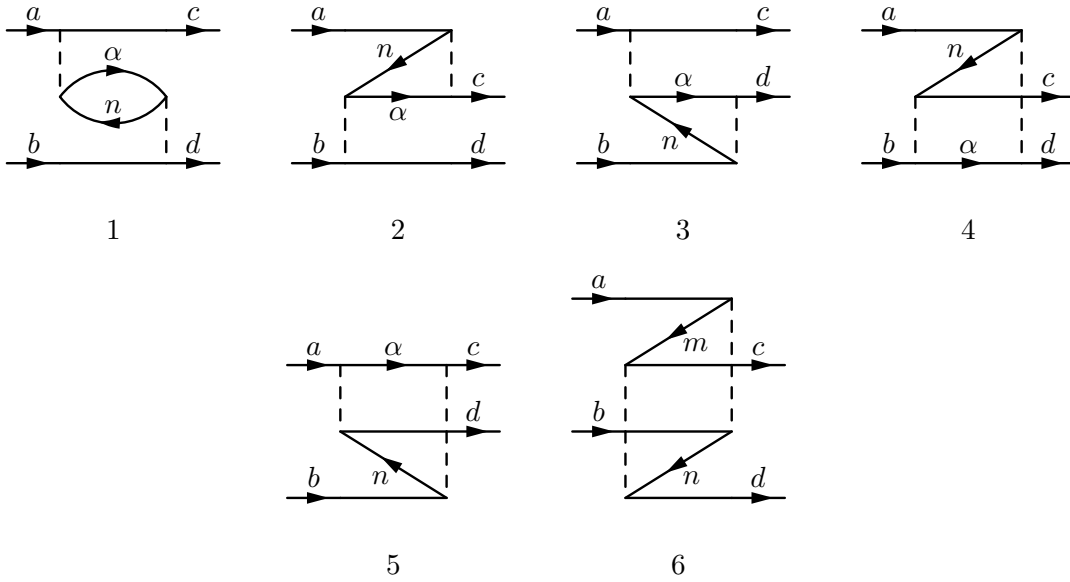
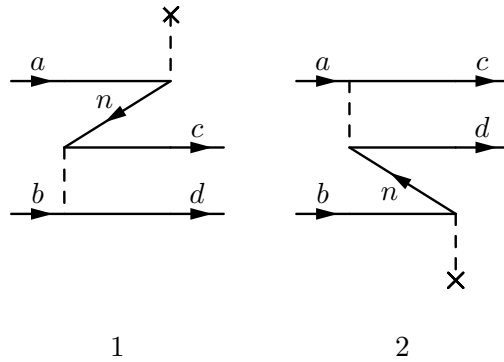


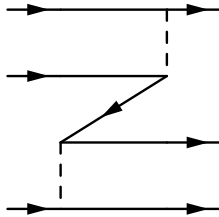
FIG. 4: $\Sigma^{(2)}$ subtraction diagrams. Each has a complementary mirror-image partner.



It is worth noting also that the two-body diagrams with the largest contribution to the energy (the direct diagram, Fig. 3.1, and its mirror) make no (linear) contribution to the SMS because they cancel. The exchange diagrams do contribute to the SMS; nevertheless, it is because of this cancellation that the contribution of $\Sigma^{(2)}$ to k_{SMS} is generally smaller than that of $\Sigma^{(1)}$.

Figure 5 shows a diagram with three external lines, $\Sigma^{(3)}$, where three valence electrons interact via the core. The diagrams of this type are easy to calculate (having only one internal summation and no summations over virtual states), but the number of corresponding effective radial integrals is huge. To include this diagram everywhere in the CI calculation would involve taking into account not only corrections to $\mathcal{H}^{(1)}$ and $\mathcal{H}^{(2)}$, but it would also introduce an effective $\mathcal{H}^{(3)}$. Fortunately, as explained in Ref. [17], it is possible to omit these diagrams entirely provided that one makes an appropriate choice of the atomic core. We have not included $\Sigma^{(3)}$ in this paper.

FIG. 5: Effective three-valence-electron interaction of Σ_2 .



Analytical expressions for the diagrams of Figs. 1 – 4 are given in Appendix B.

A final point worth mentioning is the definition of the energy denominators in the expressions corresponding to the diagrams. Our formalism corresponds to Brillouin-Wigner perturbation theory, and so there is an explicit dependence on the energy of the whole atom: E in Eqs. (17) and (27).

From Eq. (13), $E = E_{\text{core}} + E_{\text{val}}$, and so the core part cancels in the energy denominator $E - \mathcal{H}_0$ (see Eq. (23)). The energy E_{val} corresponds to the energy of all the valence electrons. To calculate \mathcal{H}_0 , however, one should take into account the state of all valence electrons for each disconnected diagram. This is computationally impractical, but again one can simplify. In this paper all connected diagrams are evaluated at the energies which correspond to the main configuration. For example, when calculating Fig. 1.1 the usual Rayleigh-Shrödinger perturbation theory would give the denominator $(\epsilon_a + \epsilon_n - \epsilon_\alpha - \epsilon_\beta)$; we instead use $(\epsilon_{2s} + \epsilon_n - \epsilon_\alpha - \epsilon_\beta)$ if a and b are s -wave, or $(\epsilon_{2p_{1/2}} + \epsilon_n - \epsilon_\alpha - \epsilon_\beta)$ if a is p -wave, and so on.

The Brillouin-Wigner formalism used in our method has two major advantages over the Rayleigh-Shrödinger perturbation theory. Firstly, we wish to preserve the symmetry of the CI matrix when Σ is added, so we cannot have an energy denominator that depends on which state is initial and which is final. Secondly, Rayleigh-Shrödinger theory does not allow a large P space as it will produce small denominators for excited configurations. That is known to lead to “intruder states” – unphysical states that can lie even below the ground state. By contrast, Brillouin-Wigner theory is known to have the wrong limit for an infinite number of valence electrons. It is possible to formulate the theory without these drawbacks by modifying E (Ref. [23]). However, the energy dependence of the effective Hamiltonian is a higher order effect; compared to the prescription above, it leads to a relatively small energy correction that we neglect.

IV. CALCULATIONS AND RESULTS

We present results for each species of carbon separately, in order of increasing number of valence electrons. For all calculations we use a relativistic B-spline single-electron basis set similar to that developed by Johnson *et al.*[24, 25, 26]. In all cases the MBPT calculation considers $1s^2$ as the core, and all other states as valence. We have used two different B-spline basis sets, each with a different number of shells included in the self-consistent Dirac-Fock procedure. The first set, \mathcal{B}_1 , is formed in the potential of the closed shell $1s^2$ core; this corresponds to $N_{\text{DF}} = N_{\text{core}}$. For this set the subtraction diagrams of Figs. 2 and 4 are zero.

The second basis set, \mathcal{B}_2 , is formed in the potential of the $1s^2 2s^2$ core; thus $N_{\text{DF}} > N_{\text{core}}$ and the subtraction diagrams must be included.

The basis sets are described by giving the largest principal quantum number for each wave, e.g. $8spd6f$ includes the orbitals $1 - 8s_{1/2}$, $2 - 8p_j$, $3 - 8d_j$, and $4 - 6f_j$. For the MBPT we have used the basis $40spdfg$ for all ions. This basis is fully saturated in the sense that the energies and isotope shifts do not change with the addition of more basis functions.

A. CIV

CIV has one electron above a closed $1s^2$ core. It can therefore be treated as a single valence electron atom using MBPT, or as a three electron atom using CI. We have used both methods; the results are presented for comparison in Table I. In each case, the calculations were done using the \mathcal{B}_1 basis set. The isotope shift results have also been compared with previous theoretical approaches. Multiconfiguration Hartree-Fock – CI calculations were presented in Ref. [13], which also combined the Hylleraas and full-core plus correlation (FCPC) calculations of Refs. [27] and [28] respectively.

TABLE I: Comparison of energies and k_{SMS} transitions from the ground state in CIV using various methods. The transition energies presented do not include the addition of mass shift effects. Note that all results presented by other groups are non-relativistic and hence do not distinguish fine-structure.

Level	Energy DF + $\Sigma^{(1)}$ (expt.)	Full CI	Other works
	Energy (cm^{-1})		
$2p \ ^2P_{1/2}^o$	64484	64551	64594 ^a 64564 ^a
$2p \ ^2P_{3/2}^o$	64592	64681	64725 ^b 64449 ^c
	k_{SMS} (GHz·amu)		
$2p \ ^2P_{1/2}^o$		-4511	-4521 ^a -4526 ^a
$2p \ ^2P_{3/2}^o$		-4504	-4514 ^b -4528 ^c

^aMCHF–CI: Carlsson *et al.*, 1995 [13]

^bMCHF: Godefroid *et al.*, 2001 [14]

^cHylleraas + FCPC: Results of King, 1989 [27], and Wang *et al.*, 1993 [28], combined and presented in Ref. [13]

As noted previously, the MBPT basis was completely saturated, however we have only included second order diagrams in our calculation. By contrast, the CI calculations are complete (although they do not include the Breit interaction and QED effects), but the basis is not completely saturated. We have used an effective $22spd8f$ basis for the CI calculation, including only single and double excitations from the leading configurations (SD-CI). We included triple excitations for a smaller basis, $14spd8f$: this made a difference of less than 2 cm^{-1} in the transition energy, and less than 1 GHz·amu for k_{SMS} . Other f -wave and higher partial waves were also found to be unimportant.

All methods give the same value for the transition energies and SMS constants to within 0.5%.

B. C III

The ground state for C III is $1s^2 2s^2 \ ^1S_0$. We have done our calculations both as a four-electron CI problem (full CI) and by combining two-valence-electron CI with MBPT, considering $1s^2$ as the frozen core (CI + $\Sigma^{(1,2)}$). All results are presented in Table II. Also included are CI results (the pure two-electron CI method) and CI + $\Sigma^{(1)}$ results (that do not include $\Sigma^{(2)}$). This allows us to examine the roles of the different parts of the core-correlation. The CI and CI + $\Sigma^{(1)}$ results are calculated with the \mathcal{B}_2 basis set; the complete CI + $\Sigma^{(1,2)}$ results have been calculated using both the \mathcal{B}_1 and \mathcal{B}_2 sets. Additionally we have presented the MCHF results of Ref. [15].

TABLE II: Comparison of energies, k_{SMS} , and q -values for transitions from the ground state in C III using various methods. Note that the MCHF results are non-relativistic and hence do not distinguish fine-structure.

Level	Energy (expt.)	CI	CI + $\Sigma^{(1)}$	CI + $\Sigma^{(1,2)}$		Full CI	MCHF ^a
				\mathcal{B}_2	\mathcal{B}_1		
Energy (cm ⁻¹)							
$2s2p \ ^3P_0^o$	52367	52750	52322	52349	52383	52506	52280
$2s2p \ ^3P_1^o$	52391	52784	52357	52383	52418	52534	
$2s2p \ ^3P_2^o$	52447	52852	52427	52453	52488	52592	
$2s2p \ ^1P_1^o$	102352	103719	103365	102725	102775	103109	102598
k_{SMS} (GHz·amu)							
$2s2p \ ^3P_0^o$		-3439	-3478	-3473	-3470	-3483	-3475
$2s2p \ ^3P_1^o$		-3438	-3476	-3472	-3468	-3480	
$2s2p \ ^3P_2^o$		-3434	-3473	-3468	-3465	-3474	
$2s2p \ ^1P_1^o$		-2688	-2759	-2790	-2784	-2882	-2817
q (cm ⁻¹)							
$2s2p \ ^3P_0^o$		75	74	74			
$2s2p \ ^3P_1^o$		109	108	108			
$2s2p \ ^3P_2^o$		177	178	178			
$2s2p \ ^1P_1^o$		165	165	165			

^aJönsson *et al.*, 1999 [15]

For the full four-electron CI method we used a very large basis $16spdf$, in the SD-CI approximation. This was not enough to saturate the basis entirely, and we could go no further because the Hamiltonian matrix became too large. The error in k_{SMS} from the full CI calculation could be as large as 100 GHz·amu. Nonetheless, they are in agreement with the calculations of Ref. [15], as well as the results of our own CI + MBPT.

The CI + MBPT method is particularly accurate for C III for two reasons. Firstly, because there are only two valence electrons there are no triple excitations, which keeps the

Hamiltonian small without the need for approximations (for ions with more valence electrons we have used the SD-CI approximation). Because the Hamiltonian is relatively small, we can completely saturate the basis at $20spdf$. Also, there is no $\Sigma^{(3)}$ (corresponding to Fig. 5); as stated before, in this paper we have not included it anyway. These points hold true for all two-valence-electron atoms; in particular we have previously shown that excellent results are attainable for MgI (Ref. [19]).

In Ref. [15] the MCHF results were given an error of 1%; our CI + MBPT results are within this range, and so we believe that we have obtained a similar accuracy. It is also worth noting again that we have excluded the extra box diagrams with “wrong” parity from the results presented. The inclusion of these diagrams in $\Sigma^{(2)}$ makes a difference of around 0.1% to the k_{SMS} constants.

C. C II

We have treated C II as a three-valence-electron ion; its ground state is $2s^22p\ ^2P_{1/2}^o$. We have used the \mathcal{B}_2 basis $20spdf$, which corresponds to the V^{N-1} potential, and we have restricted ourselves in the CI problem to single and double excitations from the leading configurations $2s^22p$ and $2s2p^2$.

In Table III we present all results for C II. Again we have presented the breakdown of the various parts of the CI + MBPT method. We have also performed our calculations using the \mathcal{B}_1 basis: this changed the results by less than 1% for all results except for the $^2S_{1/2}$ transition, in which the difference was around 3%. For this transition, neither basis set was enough to completely saturate k_{SMS} . Furthermore, the difference between the results of CI + MBPT and MCHF-CI is fairly large for this transition (around 7%). Adding the next most important configuration, $2s^23s$, to the leading set changes the energy of the $^2S_{1/2}$ transition by 30 cm^{-1} (0.03%) and k_{SMS} by $14\text{ GHz}\cdot\text{amu}$ (around 1%). The effect on all other transitions was much smaller.

D. C I

In Table IV we present energies for transitions in neutral carbon. The ground state of C I is $2s^22p^2\ ^3P_0$. We used the \mathcal{B}_2 basis of size $16spdf$, and took all single and double excitations from several leading configurations. The energies obtained for this atom are not as good as those of the other ions. It is testimony to the power of the B-spline basis, however, that the levels appear in the correct order (with the exception of some fine structure), which is remarkable considering that the spectrum is very dense.

We have generated q -values for C I because the previous calculations (Ref. [29]) had large uncertainties. We believe the new values, presented in Table IV, have errors of around 10 cm^{-1} .

In Table V we present the SMS constants for C I. We are within 1% of the values obtained using the MCHF-CI method (Refs. [13] and [16]). For most transitions the effect of core-correlations on k_{SMS} is around 1 or 2%, however in some cases they are larger (for example, in $2s2p^3\ ^3P^o$ the core correlations are 8% of the total).

TABLE IV: Comparison of energies and q -values for transitions from the ground state in CI using various methods. Note that the MCHF–CI results are non-relativistic and hence do not distinguish fine-structure.

Level	Energy (cm ⁻¹)				q (cm ⁻¹)		
	(expt.)	CI	CI + $\Sigma^{(1)}$	CI + $\Sigma^{(1,2)}$	MCHF–CI	CI + $\Sigma^{(1,2)}$	CI ^a
$2s^2 2p^2 \ ^1S_0$	21648	22140	22213	22335	21753 ^b	38	
$2s 2p^3 \ ^5S_2^o$	33735	33529	33234	33240	33498 ^b	146	
$2s^2 2p 3s \ ^3P_0^o$	60333	59806	60182	60144		-47	
$2s^2 2p 3s \ ^3P_1^o$	60353	59826	60202	60164		-24	
$2s^2 2p 3s \ ^3P_2^o$	60393	59866	60243	60206		26	
$2s^2 2p 3s \ ^1P_1^o$	61982	61587	61975	61911	62002 ^b	1	
$2s 2p^3 \ ^3D_3^o$	64087	64773	64628	64562		144	151(60)
$2s 2p^3 \ ^3D_1^o$	64090	64762	64617	64551	64036 ^c	137	141(60)
$2s 2p^3 \ ^3D_2^o$	64091	64766	64622	64555		140	145(60)
$2s 2p^3 \ ^3P_1^o$	75254	76209	76196	76153		117	111(60)
$2s 2p^3 \ ^3P_2^o$	75255	76214	76202	76158		121	
$2s 2p^3 \ ^3P_0^o$	75256	76207	76194	76151		115	
$2s^2 2p 3d \ ^1D_2^o$	77680	79297	79724	79643		7	
$2s^2 2p 4s \ ^3P_0^o$	78105	79737	80152	80076		-33	
$2s^2 2p 4s \ ^3P_1^o$	78117	79750	80166	80090		-21	
$2s^2 2p 4s \ ^3P_2^o$	78148	79787	80205	80130		24	
$2s^2 2p 3d \ ^3F_2^o$	78199	79845	80271	80193		-31	
$2s^2 2p 3d \ ^3F_3^o$	78216	79862	80289	80211		-18	
$2s^2 2p 3d \ ^3D_1^o$	78293	79937	80354	80275		-13	
$2s^2 2p 3d \ ^3D_2^o$	78308	79954	80371	80293		13	
$2s^2 2p 3d \ ^3D_3^o$	78318	79966	80385	80306		29	
$2s^2 2p 4s \ ^1P_1^o$	78340	79983	80403	80327		17	
$2s^2 2p 3d \ ^1F_3^o$	78530	80802	80626	80549		15	
$2s^2 2p 3d \ ^1P_1^o$	78731	80402	80822	80746		12	
$2s^2 2p 3d \ ^3P_2^o$	79311	80957	81307	81225		18	
$2s^2 2p 3d \ ^3P_1^o$	79319	80967	81318	81237		30	
$2s^2 2p 3d \ ^3P_0^o$	79323	80972	81323	81242		35	
$2s^2 2p 4d \ ^1D_2^o$	83498	86521	86942	86858		8	

^aBerengut *et al.*, 2004 [29]

^bCarlsson *et al.*, 1995 [13]

^cJönsson *et al.*, 1996 [16]

within a few percent. In Table VI we compare our calculations with the few experiments that exist for carbon ions; in all cases agreement is within around 0.005 cm⁻¹, which corresponds to an error in k_{SMS} of around 20 GHz·amu.

In Table VII we present total isotope shifts for some important transitions. These transitions can be observed in quasar absorption spectra, and can therefore be used to probe variation of α and isotope abundance evolution. The results are presented both in MHz and km/sec: the latter is the preferred form for use in astronomy.

TABLE V: Comparison of k_{SMS} for transitions from the ground state in CI using various methods. Note that the MCHF–CI results are non-relativistic and hence do not distinguish fine-structure.

Level	Energy (expt.)	k_{SMS} (GHz·amu)			MCHF–CI
		CI	CI + $\Sigma^{(1)}$	CI + $\Sigma^{(1,2)}$	
$2s^2 2p^2 \ ^1S_0$	21648	186	180	191	152 ^a
$2s 2p^3 \ ^5S_2^o$	33735	-2540	-2579	-2588	-2583 ^a
$2s^2 2p 3s \ ^3P_0^o$	60333	1405	1405	1419	
$2s^2 2p 3s \ ^3P_1^o$	60353	1406	1406	1420	
$2s^2 2p 3s \ ^3P_2^o$	60393	1408	1408	1422	
$2s^2 2p 3s \ ^1P_1^o$	61982	1549	1551	1559	1553 ^a
$2s 2p^3 \ ^3D_3^o$	64087	-2165	-2224	-2227	
$2s 2p^3 \ ^3D_1^o$	64090	-2165	-2224	-2227	-2222 ^b
$2s 2p^3 \ ^3D_2^o$	64091	-2165	-2224	-2227	
$2s 2p^3 \ ^3P_1^o$	75254	-1272	-1390	-1392	
$2s 2p^3 \ ^3P_2^o$	75255	-1272	-1389	-1391	
$2s 2p^3 \ ^3P_0^o$	75256	-1271	-1390	-1392	
$2s^2 2p 3d \ ^1D_2^o$	77680	1334	1320	1331	
$2s^2 2p 4s \ ^3P_0^o$	78105	1398	1392	1407	
$2s^2 2p 4s \ ^3P_1^o$	78117	1404	1397	1412	
$2s^2 2p 4s \ ^3P_2^o$	78148	1415	1408	1422	
$2s^2 2p 3d \ ^3F_2^o$	78199	1378	1368	1381	
$2s^2 2p 3d \ ^3F_3^o$	78216	1381	1372	1384	
$2s^2 2p 3d \ ^3D_1^o$	78293	1430	1422	1434	
$2s^2 2p 3d \ ^3D_2^o$	78308	1429	1421	1432	
$2s^2 2p 3d \ ^3D_3^o$	78318	1430	1420	1432	
$2s^2 2p 4s \ ^1P_1^o$	78340	1443	1435	1446	
$2s^2 2p 3d \ ^1F_3^o$	78530	1451	1440	1452	
$2s^2 2p 3d \ ^1P_1^o$	78731	1436	1426	1438	
$2s^2 2p 3d \ ^3P_2^o$	79311	948	998	1010	
$2s^2 2p 3d \ ^3P_1^o$	79319	956	1006	1018	
$2s^2 2p 3d \ ^3P_0^o$	79323	960	1009	1021	
$2s^2 2p 4d \ ^1D_2^o$	83498	1277	1258	1268	

^aCarlsson *et al.*, 1995 [13]

^bJönsson *et al.*, 1995 [16]

VI. ACKNOWLEDGEMENTS

This work is supported by the Australian Research Council; Department of Energy, Office of Nuclear Physics, Contract No. W-31-109-ENG-38; Gordon Godfrey fund; and Russian Foundation for Basic Research, grant No. 05-02-16914. The authors would like to thank V. A. Dzuba for useful discussions. We are grateful to the APAC National Facility for providing computer time.

TABLE VI: Comparison of calculated $^{13}\text{C} - ^{12}\text{C}$ isotope shifts with experiment.

Transition		λ	$\delta\nu^{13,12}$ (cm^{-1})	
Lower Level	Upper Level	(\AA)	Expt.	This work
C I				
$2s^2 2p^2 \ ^3P_2$	$2s 2p^3 \ ^5S_2^o$	2967	$0.670(5)^a$	0.674^b
$2s^2 2p^2 \ ^1S_0$	$2s^2 2p 3s \ ^1P_1^o$	2479	$-0.156(3)^c$	-0.151
			$-0.156(2)^d$	
C II				
$2s 2p^2 \ ^2S_{1/2}$	$2s^2 3p \ ^2P_{3/2}^o$	2837	$-0.612(2)^c$	-0.617
$2s 2p^2 \ ^2S_{1/2}$	$2s^2 3p \ ^2P_{1/2}^o$	2838	$-0.623(3)^c$	-0.617

^aBernheim and Kittrell, 1980 [30]

^bActually, the $2s^2 2p^2 \ ^3P_0 - 2s 2p^3 \ ^5S_2^o$ transition was calculated.

^cBurnett, 1950 [31]

^dHolmes, 1951 [32]

 TABLE VII: Total $^{13}\text{C} - ^{12}\text{C}$ and $^{14}\text{C} - ^{12}\text{C}$ isotope shifts for important transitions. We believe the errors are of the order of 0.1 GHz.

Transition		λ	$\delta\nu^{13,12}$		$\delta\nu^{14,12}$	
Ground State	Upper Level	(\AA)	(GHz)	(km/sec) ^a	(GHz)	(km/sec) ^a
C I						
$2s^2 2p^2 \ ^3P_0$	$2s^2 2p 3s \ ^3P_1^o$	1657	-2.75	0.46	-5.09	0.84
	$2s 2p^3 \ ^3D_1^o$	1560	21.10	-3.29	39.12	-6.10
	$2s 2p^3 \ ^3P_1^o$	1329	16.91	-2.25	31.34	-4.17
	$2s^2 2p 4s \ ^3P_1^o$	1280	-0.82	0.10	-1.51	0.19
	$2s^2 2p 3d \ ^3D_1^o$	1277	-0.94	0.12	-1.75	0.22
	$2s^2 2p 4s \ ^1P_1^o$	1276	-1.01	0.13	-1.88	0.24
	$2s^2 2p 3d \ ^3P_1^o$	1261	1.84	-0.23	3.42	-0.43
C II						
$2s^2 2p \ ^2P_{1/2}^o$	$2s 2p^2 \ ^2D_{3/2}$	1336	25.10	-3.35	46.53	-6.21
	$2s 2p^2 \ ^2D_{5/2}$	1336	25.10	-3.35	46.54	-6.21
	$2s 2p^2 \ ^2S_{1/2}$	1037	18.70	-1.94	34.66	-3.59
C III						
$2s^2 \ ^1S_0$	$2s 2p \ ^1P_1^o$	977	28.76	-2.81	53.33	-5.21
C IV						
$2s \ ^2S_{1/2}$	$2p \ ^2P_{1/2}^o$	1551	35.89	-5.57	66.54	-10.32
	$2p \ ^2P_{3/2}^o$	1548	35.79	-5.54	66.35	-10.27

^a $\delta\nu = \delta\lambda/\lambda \times c$ (km/sec). A negative velocity means that ^{14}C (and ^{13}C) are at lower wavelength than ^{12}C .

APPENDIX A: MATRIX ELEMENT OF THE TWO-BODY OPERATOR

The two-body operator used in this work is the sum of the Coulomb interaction operator and the “rescaled” SMS operator (atomic units):

$$\tilde{Q} = \frac{1}{|\mathbf{r}_1 - \mathbf{r}_2|} + \lambda \mathbf{p}_1 \cdot \mathbf{p}_2 \equiv \sum_k \tilde{Q}_k, \quad (\text{A1})$$

where λ is the scaling factor, $\mathbf{p} = -i\nabla$ is electron momentum, and

$$\tilde{Q}_k = \frac{4\pi}{2k+1} \frac{r_{\leq}^k}{r_{>}^{k+1}} Y_k(\mathbf{n}_1) Y_k(\mathbf{n}_2) + \lambda \mathbf{p}_1 \cdot \mathbf{p}_2 \delta_{k1}. \quad (\text{A2})$$

We use the following form for the single-electron wave function

$$\phi(\mathbf{r})_{jlm} = \frac{1}{r} \begin{pmatrix} f(r)\Omega(\mathbf{n})_{jlm} \\ i\alpha g(r)\tilde{\Omega}(\mathbf{n})_{jlm} \end{pmatrix}. \quad (\text{A3})$$

Here $\alpha = 1/137.036$ is the fine structure constant, and $\tilde{\Omega}(\mathbf{n})_{jlm} = -(\vec{\sigma} \cdot \mathbf{n})\Omega(\mathbf{n})_{jlm}$.

The matrix element of operator (A2) with wave functions (A3) has the form

$$\langle \phi_a(\mathbf{r}_1)\phi_b(\mathbf{r}_2) | \tilde{Q}_k | \phi_c(\mathbf{r}_1)\phi_d(\mathbf{r}_2) \rangle = C_{ab,cd}^k (R_{ab,cd}^k - \lambda \delta_{k1} p_{ac} p_{bd}), \quad (\text{A4})$$

where the angular factor C_k is the same for both operators

$$\begin{aligned} C_{ab,cd}^k &= (-1)^{q+m_a+m_b} \begin{pmatrix} j_a & k & j_c \\ -m_a & q & m_c \end{pmatrix} \begin{pmatrix} j_b & k & j_d \\ -m_b & -q & m_d \end{pmatrix} \\ &\times (-1)^{j_a+j_b+j_c+j_d+1} \sqrt{(2j_a+1)(2j_b+1)(2j_c+1)(2j_d+1)} \\ &\times \begin{pmatrix} j_a & j_c & k \\ \frac{1}{2} & -\frac{1}{2} & 0 \end{pmatrix} \begin{pmatrix} j_b & j_d & k \\ \frac{1}{2} & -\frac{1}{2} & 0 \end{pmatrix} \xi(l_a+l_c+k)\xi(l_b+l_d+k), \\ \xi(x) &= \begin{cases} 1, & \text{if } x \text{ is even} \\ 0, & \text{if } x \text{ is odd} \end{cases}, \end{aligned} \quad (\text{A5})$$

$R_{ab,cd}^k$ is radial Coulomb integral

$$R_{ab,cd}^k = \int_0^\infty \frac{r_{\leq}^k}{r_{>}^{k+1}} \left(f_a(r_1)f_c(r_1) + \alpha^2 g_a(r_1)g_c(r_1) \right) \left(f_b(r_2)f_d(r_2) + \alpha^2 g_b(r_2)g_d(r_2) \right) dr_1 dr_2, \quad (\text{A6})$$

while p_{12} is the radial matrix element of the SMS operator

$$\begin{aligned} p_{12} &= A_{12}\delta_{l_1 l_2 + 1} + B_{12}\delta_{l_1 l_2 - 1}, \\ A_{12} &= \int_0^\infty f_1 \left(\frac{d}{dr} - \frac{l_1}{r} \right) f_2 dr, \\ B_{12} &= \int_0^\infty f_1 \left(\frac{d}{dr} + \frac{l_2}{r} \right) f_2 dr. \end{aligned} \quad (\text{A7})$$

APPENDIX B: EFFECTIVE INTEGRALS FOR Σ DIAGRAMS

Here we give expressions for the diagrams in Figs. 1 – 4. The following conventions for the indices are used: a, b, c , and d correspond to the external lines (valence electrons); $1 \leq m, n \leq N_{\text{core}}$; $N_{\text{core}} + 1 \leq \alpha, \beta$. Following [22] we use the shorthand notation $[j, k, \dots] = (2j+1)(2k+1)\dots$. Note also that all Wigner three- j symbols come with a parity selection rule, which is not explicitly given. This is because the three- j terms come from the formula

$$-[l_1, l_2]^{1/2} \begin{pmatrix} l_1 & k & l_2 \\ 0 & 0 & 0 \end{pmatrix} \begin{Bmatrix} j_1 & j_2 & k \\ l_2 & l_1 & k \end{Bmatrix} = \begin{pmatrix} j_1 & j_2 & k \\ 1/2 & -1/2 & 0 \end{pmatrix} \xi(l_1 + l_2 + k).$$

Additionally, the subtraction diagrams (Figs. 2 and 4) have terms which are matrix elements of h^{CI} (see Eq. (14)). This operator cannot change the angular momentum of the state; for example $\langle a | h^{\text{CI}} | n \rangle$ comes with a factor $\delta_{j_a j_n} \delta_{l_a l_n}$ which is not presented explicitly.

We start with the contributions to the self-energy matrix elements from the diagrams of Figs. 1 and 2. All of these expressions have the following additional terms that we do not write explicitly: $\delta_{j_a j_b}$, $\delta_{m_a m_b}$, and $\delta_{l_a l_b}$.

Fig. 1.1:

$$D_{a,b} = \sum_{\substack{n\alpha\beta \\ k}} \frac{[j_n, j_\alpha, j_\beta]}{[k]} \begin{pmatrix} j_a & j_\beta & k \\ 1/2 & -1/2 & 0 \end{pmatrix}^2 \begin{pmatrix} j_n & j_\alpha & k \\ 1/2 & -1/2 & 0 \end{pmatrix}^2 \frac{R_{an,\beta\alpha}^k R_{\beta\alpha,bn}^k}{\epsilon_a + \epsilon_n - \epsilon_\alpha - \epsilon_\beta} \quad (\text{B1})$$

Fig. 1.2:

$$D_{a,b} = \sum_{\substack{n\alpha\beta \\ k_1 k_2}} (-1)^{k_1+k_2} [j_n, j_\alpha, j_\beta] \begin{pmatrix} j_a & j_\beta & k_1 \\ 1/2 & -1/2 & 0 \end{pmatrix} \begin{pmatrix} j_n & j_\alpha & k_1 \\ 1/2 & -1/2 & 0 \end{pmatrix} \begin{pmatrix} j_\beta & j_n & k_2 \\ 1/2 & -1/2 & 0 \end{pmatrix} \\ \times \begin{pmatrix} j_\alpha & j_a & k_2 \\ 1/2 & -1/2 & 0 \end{pmatrix} \begin{Bmatrix} j_a & j_\beta & k_2 \\ j_n & j_\alpha & k_1 \end{Bmatrix} \frac{R_{an,\beta\alpha}^{k_1} R_{\beta\alpha,nb}^{k_2}}{\epsilon_a + \epsilon_n - \epsilon_\alpha - \epsilon_\beta} \quad (\text{B2})$$

Fig. 1.3:

$$D_{a,b} = - \sum_{\substack{mn\alpha \\ k}} \frac{[j_m, j_n, j_\alpha]}{[k]} \begin{pmatrix} j_a & j_m & k \\ 1/2 & -1/2 & 0 \end{pmatrix}^2 \begin{pmatrix} j_n & j_\alpha & k \\ 1/2 & -1/2 & 0 \end{pmatrix}^2 \frac{R_{a\alpha,mn}^k R_{mn,b\alpha}^k}{\epsilon_m + \epsilon_n - \epsilon_\alpha - \epsilon_b} \quad (\text{B3})$$

Fig. 1.4:

$$D_{a,b} = \sum_{\substack{mn\alpha \\ k_1 k_2}} (-1)^{k_1+k_2+1} [j_m, j_n, j_\alpha] \begin{pmatrix} j_a & j_m & k_1 \\ 1/2 & -1/2 & 0 \end{pmatrix} \begin{pmatrix} j_\alpha & j_n & k_1 \\ 1/2 & -1/2 & 0 \end{pmatrix} \begin{pmatrix} j_m & j_\alpha & k_2 \\ 1/2 & -1/2 & 0 \end{pmatrix} \\ \times \begin{pmatrix} j_n & j_a & k_2 \\ 1/2 & -1/2 & 0 \end{pmatrix} \begin{Bmatrix} j_a & j_n & k_2 \\ j_\alpha & j_m & k_1 \end{Bmatrix} \frac{R_{a\alpha,mn}^{k_1} R_{mn,ab}^{k_2}}{\epsilon_m + \epsilon_n - \epsilon_\alpha - \epsilon_b} \quad (\text{B4})$$

Fig. 2.1:

$$D_{a,b} = \sum_{n\alpha} [j_n] \frac{R_{an,b\alpha}^0 \langle n | h^{\text{CI}} | \alpha \rangle}{\epsilon_n - \epsilon_\alpha} \quad (\text{B5})$$

Fig. 2.2:

$$D_{a,b} = \sum_{\substack{n\alpha \\ k}} (-1)^{2j_a} [j_n] \begin{pmatrix} j_a & j_n & k \\ 1/2 & -1/2 & 0 \end{pmatrix}^2 \frac{R_{a\alpha,nb}^k \langle n | h^{\text{CI}} | \alpha \rangle}{\epsilon_n - \epsilon_\alpha} \quad (\text{B6})$$

Fig. 2.3:

$$D_{a,b} = - \sum_n \frac{\langle a | h^{\text{CI}} | n \rangle \langle n | h^{\text{CI}} | b \rangle}{\epsilon_n - \epsilon_a} \quad (\text{B7})$$

Next we present contributions to the valence-valence screening diagrams due to the diagrams of Figs. 3 and 4. These diagrams have k as an external parameter (not to be summed over). In the CI procedure they are added to $R_{ab,cd}^k$ of Eq. (A4).

Fig. 3.1:

$$R_{ab,cd}^k = \sum_{n\alpha} \frac{[j_\alpha, j_n]}{[k]} \begin{pmatrix} j_\alpha & j_n & k \\ 1/2 & -1/2 & 0 \end{pmatrix}^2 \frac{R_{an,\alpha}^k R_{cb,nd}^k}{\epsilon_\alpha - \epsilon_n} \quad (\text{B8})$$

Fig. 3.2:

$$R_{ab,cd}^k = \sum_{\substack{n\alpha \\ k_1}} (-1)^{k_1+k} [j_\alpha, j_n] \begin{pmatrix} j_a & j_n & k_1 \\ 1/2 & -1/2 & 0 \end{pmatrix} \begin{pmatrix} j_\alpha & j_c & k_1 \\ 1/2 & -1/2 & 0 \end{pmatrix} \begin{pmatrix} j_n & j_\alpha & k \\ 1/2 & -1/2 & 0 \end{pmatrix} \\ \times \begin{pmatrix} j_a & j_c & k \\ 1/2 & -1/2 & 0 \end{pmatrix}^{-1} \left\{ \begin{matrix} j_a & j_c & k \\ j_\alpha & j_n & k_1 \end{matrix} \right\} \frac{R_{a\alpha,nc}^{k_1} R_{nb,\alpha d}^k}{\epsilon_n - \epsilon_\alpha} \quad (\text{B9})$$

Fig. 3.3:

$$R_{ab,cd}^k = \sum_{\substack{n\alpha \\ k_1}} (-1)^{k_1+k} [j_\alpha, j_n] \begin{pmatrix} j_b & j_n & k_1 \\ 1/2 & -1/2 & 0 \end{pmatrix} \begin{pmatrix} j_\alpha & j_d & k_1 \\ 1/2 & -1/2 & 0 \end{pmatrix} \begin{pmatrix} j_n & j_\alpha & k \\ 1/2 & -1/2 & 0 \end{pmatrix} \\ \times \begin{pmatrix} j_b & j_d & k \\ 1/2 & -1/2 & 0 \end{pmatrix}^{-1} \left\{ \begin{matrix} j_b & j_d & k \\ j_\alpha & j_n & k_1 \end{matrix} \right\} \frac{R_{b\alpha,nd}^{k_1} R_{na,\alpha c}^k}{\epsilon_n - \epsilon_\alpha} \quad (\text{B10})$$

Fig. 3.4:

$$R_{ab,cd}^k = \sum_{\substack{n\alpha \\ k_1 k_2}} (-1)^{j_a+j_b+j_c+j_d+j_\alpha+j_n} [j_\alpha, j_n, k] \begin{pmatrix} j_a & j_n & k_1 \\ 1/2 & -1/2 & 0 \end{pmatrix} \begin{pmatrix} j_\alpha & j_d & k_1 \\ 1/2 & -1/2 & 0 \end{pmatrix} \\ \times \begin{pmatrix} j_n & j_c & k_2 \\ 1/2 & -1/2 & 0 \end{pmatrix} \begin{pmatrix} j_b & j_\alpha & k_2 \\ 1/2 & -1/2 & 0 \end{pmatrix} \begin{pmatrix} j_a & j_c & k \\ 1/2 & -1/2 & 0 \end{pmatrix}^{-1} \begin{pmatrix} j_b & j_d & k \\ 1/2 & -1/2 & 0 \end{pmatrix}^{-1} \\ \times \left\{ \begin{matrix} j_c & j_a & k \\ k_1 & k_2 & j_n \end{matrix} \right\} \left\{ \begin{matrix} j_b & j_d & k \\ k_1 & k_2 & j_\alpha \end{matrix} \right\} \frac{R_{a\alpha,nd}^{k_1} R_{nb,\alpha c}^{k_2}}{\epsilon_n - \epsilon_\alpha} \quad (\text{B11})$$

Fig. 3.5:

$$R_{ab,cd}^k = \sum_{\substack{n\alpha \\ k_1 k_2}} (-1)^{j_a+j_b+j_c+j_d+j_\alpha+j_n} [j_\alpha, j_n, k] \begin{pmatrix} j_a & j_\alpha & k_1 \\ 1/2 & -1/2 & 0 \end{pmatrix} \begin{pmatrix} j_n & j_d & k_1 \\ 1/2 & -1/2 & 0 \end{pmatrix} \\ \times \begin{pmatrix} j_\alpha & j_c & k_2 \\ 1/2 & -1/2 & 0 \end{pmatrix} \begin{pmatrix} j_b & j_n & k_2 \\ 1/2 & -1/2 & 0 \end{pmatrix} \begin{pmatrix} j_a & j_c & k \\ 1/2 & -1/2 & 0 \end{pmatrix}^{-1} \begin{pmatrix} j_b & j_d & k \\ 1/2 & -1/2 & 0 \end{pmatrix}^{-1} \\ \times \left\{ \begin{matrix} j_c & j_a & k \\ k_1 & k_2 & j_\alpha \end{matrix} \right\} \left\{ \begin{matrix} j_b & j_d & k \\ k_1 & k_2 & j_n \end{matrix} \right\} \frac{R_{an,\alpha d}^{k_1} R_{ab,cn}^{k_2}}{\epsilon_n - \epsilon_\alpha} \quad (\text{B12})$$

Fig. 3.6:

$$\begin{aligned}
R_{ab,cd}^k &= \sum_{\substack{mn \\ k_1 k_2}} (-1)^{j_a+j_b+j_c+j_d+j_m+j_n+k+k_1+k_2+1} [j_m, j_n, k] \begin{pmatrix} j_a & j_m & k_1 \\ 1/2 & -1/2 & 0 \end{pmatrix} \begin{pmatrix} j_b & j_n & k_1 \\ 1/2 & -1/2 & 0 \end{pmatrix} \\
&\times \begin{pmatrix} j_m & j_c & k_2 \\ 1/2 & -1/2 & 0 \end{pmatrix} \begin{pmatrix} j_n & j_d & k_2 \\ 1/2 & -1/2 & 0 \end{pmatrix} \begin{pmatrix} j_a & j_c & k \\ 1/2 & -1/2 & 0 \end{pmatrix}^{-1} \begin{pmatrix} j_b & j_d & k \\ 1/2 & -1/2 & 0 \end{pmatrix}^{-1} \\
&\times \left\{ \begin{matrix} j_c & j_a & k \\ k_1 & k_2 & j_m \end{matrix} \right\} \left\{ \begin{matrix} j_d & j_b & k \\ k_1 & k_2 & j_n \end{matrix} \right\} \frac{R_{ab,mn}^{k_1} R_{mn,cd}^{k_2}}{\epsilon_m + \epsilon_n - \epsilon_c - \epsilon_d}
\end{aligned} \tag{B13}$$

Fig. 4.1:

$$R_{ab,cd}^k = - \sum_n \frac{R_{nb,cd}^k \langle a | h^{\text{CI}} | n \rangle}{\epsilon_n - \epsilon_a} \tag{B14}$$

Fig. 4.2:

$$R_{ab,cd}^k = - \sum_n \frac{R_{an,cd}^k \langle b | h^{\text{CI}} | n \rangle}{\epsilon_n - \epsilon_b} \tag{B15}$$

- [1] J. K. Webb, V. V. Flambaum, C. W. Churchill, M. J. Drinkwater, and J. D. Barrow, *Phys. Rev. Lett.* **82**, 884 (1999).
- [2] J. K. Webb, M. T. Murphy, V. V. Flambaum, V. A. Dzuba, J. D. Barrow, C. W. Churchill, J. X. Prochaska, and A. M. Wolfe, *Phys. Rev. Lett.* **87**, 091301 (2001).
- [3] M. T. Murphy, J. K. Webb, V. V. Flambaum, V. A. Dzuba, C. W. Churchill, J. X. Prochaska, J. D. Barrow, and A. M. Wolfe, *Mon. Not. R. Astron. Soc.* **327**, 1208 (2001).
- [4] J. K. Webb, M. T. Murphy, V. V. Flambaum, and S. J. Curran, *Astrophys. Space Sci.* **283**, 565 (2003).
- [5] R. Quast, D. Reimers, and S. A. Levshakov, *Astron. Astrophys.* **414**, L7 (2004).
- [6] R. Srianand, H. Chand, P. Petitjean, and B. Aracil, *Phys. Rev. Lett.* **92**, 121302 (2004).
- [7] S. A. Levshakov, M. Centuri3n, P. Molaro, and S. D'Odorico, *Astron. Astrophys.* **434**, 827 (2005).
- [8] V. A. Dzuba, V. V. Flambaum, and J. K. Webb, *Phys. Rev. Lett.* **82**, 888 (1999).
- [9] M. G. Kozlov, V. A. Korol, J. C. Berengut, V. A. Dzuba, and V. V. Flambaum, *Phys. Rev. A* **70**, 062108 (2004).
- [10] T. P. Ashenfelter, G. J. Mathews, and K. A. Olive, *Phys. Rev. Lett.* **92**, 041102 (2004).
- [11] T. P. Ashenfelter, G. J. Mathews, and K. A. Olive, *Astrophys. J.* **615**, 82 (2004).
- [12] Y. Fenner, M. T. Murphy, and B. K. Gibson, *Mon. Not. R. Astron. Soc.* **358**, 468 (2005).
- [13] J. Carlsson, P. J3nsson, M. R. Godefroid, and C. Froese Fischer, *J. Phys. B: At. Mol. Opt. Phys.* **28**, 3729 (1995).
- [14] M. Godefroid, C. Froese Fischer, and P. J3nsson, *J. Phys. B: At. Mol. Opt. Phys.* **34**, 1079 (2001).
- [15] P. J3nsson, C. Froese Fischer, and M. R. Godefroid, *J. Phys. B: At. Mol. Opt. Phys.* **32**, 1233 (1999).
- [16] P. J3nsson, C. Froese Fischer, and M. R. Godefroid, *J. Phys. B: At. Mol. Opt. Phys.* **29**, 2393 (1996).
- [17] V. A. Dzuba, V. V. Flambaum, and M. G. Kozlov, *Phys. Rev. A* **54**, 3948 (1996).

- [18] V. A. Dzuba and W. R. Johnson, *Phys. Rev. A* **57**, 2459 (1998).
- [19] J. C. Berengut, V. V. Flambaum, and M. G. Kozlov (2005), arXiv:physics/0507062.
- [20] I. I. Sobel'man, *Atomic Spectra and Radiative Transitions* (Springer-Verlag, Berlin, 1979).
- [21] J. C. Berengut, V. A. Dzuba, and V. V. Flambaum, *Phys. Rev. A* **68**, 022502 (2003).
- [22] I. Lindgren and J. Morrison, *Atomic Many-Body Theory* (Springer-Verlag, New York, 1986).
- [23] M. G. Kozlov and S. G. Porsev, *Opt. Spectrosc.* **87**, 352 (1999).
- [24] W. R. Johnson and J. Sapirstein, *Phys. Rev. Lett.* **57**, 1126 (1986).
- [25] W. R. Johnson, M. Idrees, and J. Sapirstein, *Phys. Rev. A* **35**, 3218 (1987).
- [26] W. R. Johnson, S. A. Blundell, and J. Sapirstein, *Phys. Rev. A.* **37**, 307 (1988).
- [27] F. W. King, *Phys. Rev. A* **40**, 1735 (1989).
- [28] Z.-W. Wang, X.-W. Zhu, and K. T. Chung, *Phys. Scr.* **47**, 65 (1993).
- [29] J. C. Berengut, V. A. Dzuba, V. V. Flambaum, and M. V. Marchenko, *Phys. Rev. A* **70**, 064101 (2004).
- [30] R. A. Bernheim and C. Kittrell, *Spectrochim. Acta B* **35**, 51 (1980).
- [31] C. R. Burnett, *Phys. Rev.* **80**, 494 (1950).
- [32] J. R. Holmes, *J. Opt. Soc. Am.* **41**, 360 (1951).